Origin of strain in H+ ion implanted LiTaO3 single crystals

A. Louiset, S. Schamm-Chardon, O. Kononchuk, C. Magén, Nikolay Cherkashin

APL Materials

RESEARCH ARTICLE | NOVEMBER 13 2025

Origin of strain in H^+ ion implanted $LiTaO_3$ single crystals

A. Louiset ; S. Schamm-Chardon ; O. Kononchuk ; C. Magén ; N. Cherkashin

APL Mater. 13, 111109 (2025)
https://doi.org/10.1063/5.0291228

Origin of strain in H^+ ion implanted $LiTaO_3$ single crystals

Cite as: APL Mater. 13, 111109 (2025); doi: 10.1063/5.0291228
Submitted: 16 July 2025 • Accepted: 23 October 2025 •
Published Online: 13 November 2025

A. Louiset,[1,2] S. Schamm-Chardon,[1] O. Kononchuk,[2] C. Magén,[3] and N. Cherkashin[1,a)]

AFFILIATIONS

[1] CEMES-CNRS and Université de Toulouse, 29 Rue Jeanne Marvig, BP 94347, 31055 Toulouse Cedex 4, France
[2] Innovation, SOITEC, Parc Technologique des Fontaines, Chemin des Franques, 38190 Bernin, France
[3] Instituto de Nanociencia y Materiales de Aragón (INMA), CSIC-Universidad de Zaragoza, 50009 Zaragoza, Spain

[a)] **Author to whom correspondence should be addressed:** nikolay.cherkashin@cemes.fr

ABSTRACT

To enhance the performance of surface acoustic wave filters, industries are actively investigating the substitution of bulk lithium tantalate piezoelectric single-crystal substrates with thin films integrated onto silicon substrates. Ion implantation in these single crystals serves as the initial stage of the Smart-Cut process, widely recognized for enabling material transfer onto silicon. Identification of the physical phenomena behind ion implantation in piezoelectric single crystals remains a challenge due to the emergence of strain and, thus, local electric fields gradients. In this work, we address strain generated in $LiTaO_3$ single crystals by H^+ ion implantation in relation to the structural modifications and as a function of implanted fluence. We show that strain is not only proportional to the local H concentration, the case found in common target materials, such as Si crystals, but also proportional to the fluence with some non-linear coefficients depending on the modified elastic constants of the implanted material. We evidence that the damage redistribution is at the root of this intriguing phenomenon, which is probably linked to the emergence of gradual electric fields. Targeting a unified law for the evolution of strain with local H-concentration and H-fluence and generated damage, we provide the generalized form for fluence-normalized strain as a function of the H-to-damage concentration ratio, which is independent of fluence. Depending on the ratio range, four distinct evolutionary regimes describe the function. These are discussed in detail.

I. INTRODUCTION

Lithium tantalate ($LiTaO_3$ or LTO) piezoelectric single crystals have been used for many years as a bulk substrate for surface acoustic wave (SAW) filters, which are some of the most common radio frequency (RF) filters in mobile phones.[1] In an effort to enhance device performances, that is achieve higher frequencies, more stable operation with temperature variations, and lower energy losses in devices, industries are currently considering replacing these bulk substrates with LTO thin films integrated on a Si substrate.[2] In order to be efficient, SAW filters require a single crystal LTO thin film separated from the Si substrate by an amorphous SiO_2 layer, in a piezoelectric-on-insulator (POI) heterostructure. Unfortunately, epitaxial growth of LTO single crystals has never been achieved on any kind of a substrate.[3]

Currently, one of the most promising approaches for the fabrication of a single crystal POI is the Smart Cut™ technology.[4] This process allows performing single crystal thin film transfer by combining H^+ ion implantation and wafer bonding technologies in such a way that POIs can now be fabricated at the wafer scale.[5] Several studies have shown the superiority of the Smart Cut™ POI based devices compared to the traditional ones.[6,7]

Understanding the Smart Cut™ process physics that was developed for Si more than 30 years ago took a long time.[4] A comprehensive study was necessary until recently to fully grasp the physical phenomena and the mechanism underlying the fracture process of the H^+ ion implanted Si substrate.[8–13] Basically, Si fracture occurs due to a low solubility limit of H in Si and the presence of vacancies generated by ion implantation. Following ion implantation, they jointly precipitate in form of a wide range of relatively stable complexes. Only few of them (namely, VH_4 and V_2H_6) transform into gas filled cavities (platelets),[8,9,14] which competitively grow in line with inelastic interactions and form microcracks during thermal annealing. Besides functioning as gas sources and platelet

seeds, they generate strain gradients,[8,14,15] which have a significant effect on platelets' crystallographic orientation, subsequent inelastic interactions, and material fracture.[8,14,16,17]

The comprehension of the Smart-Cut process developed for $LiTaO_3$[18,19] remains today relatively constrained. Indeed, $LiTaO_3$ is significantly more complex than silicon, as it consists of three different atoms forming a solid solution around the stoichiometric composition ($\frac{Li}{Li+Ta}$ = 0.5). It exhibits a trigonal structure (space group R3C)[20] and possesses a spontaneous polarization aligned with the c-axis.[21] The most common composition used is the congruent one (CLT), slightly deficient in Li ($\frac{Li}{Li+Ta}$ = 0.485). As a result, it inherently exhibits a certain level of intrinsic point defects, including lithium vacancies, tantalum antisites, and tantalum interstitials.[22–24] In addition, some H is unavoidably incorporated during crystal growth in the vicinity of a Li vacancy.[25] In addition, a key distinction from silicon is that hydrogen has no solubility limit in CLT.[26–28]

Strain in H^+ ion-implanted silicon crystals arises from the material elastic reaction on the in-plane biaxial stress created by the population of (multi)vacancy hydrogenated complexes and interstitial agglomerations formed following H^+ implantation. The out-of-plane strain component remains positive, with an increase in interplanar distances perpendicular to the wafer surface.[15,29] The depth profile of the deformation has been shown to depend solely on hydrogen concentration and the elastic constants of silicon.[14]

Recent research has shed light on certain aspects of the strain configuration in CLT following H^+ ion implantation. Strain induced by H^+ ion implantation in Y-rotated LTO, especially Y42-cut LTO with 75 keV ions at fluences 1.8 to 2.2 × 10^{16} ion/cm^2, was investigated.[30] In this orientation, the deformation of (012) planes nearly parallel to the wafer surface was deemed to provide a reasonable estimate of the out-of-plane component. They also measured deformation of the (030) at −42° from the parallel to the surface. The (012) planes showed tensile deformation, while the (030) planes exhibited compressive deformation. The negative value is rather unexpected because one would expect the implanted layer to be pseudomorph to the substrate similarly to the situation observed for other implanted materials.[15,29] The study of H^+ implantation in Z-cut LTO with 180 keV ions at fluences 6×, 8× and 10× 10^{16} ions/cm^2 concluded that H^+ ion implanted mainly introduces O vacancies and H interstitials that generate strain in LTO, which increases with H fluence.[31] As far as we know, only one study has attempted to reconstruct the strain depth profiles in Z-cut LTO implanted at 110 keV with a fluence of 3 × 10^{16} cm^{-2}.[32] Damage due to nuclear interactions of the incident ion with the lattice atoms, i.e., lattice disorder and vacancy-interstitial pairs, is considered there as the origin of the localized strain. Strain depth distribution approximately follows the vacancies profile simulated by Stopping and Range of Ions in Matter (SRIM).[33]

The first two investigations cited above provide only a limited perspective on strain in implanted LTO, focusing solely on the maximum deformation along the piezoelectric axis. They do not establish any relation between hydrogen content in the implanted crystal and the induced damage. Moreover, in the third study, the resolution of XRD experiments is somewhat constrained, and the correlation between the experimental and simulated diffractograms is not entirely ideal.

This paper aims to conduct a comprehensive investigation into the effects of hydrogen ion implantation on the structural modifications of Y42-cut oriented LTO single crystals varying the total implanted fluence. This is achieved by reconstructing the full strain tensor and damage depth profiles through simulations of x-ray diffraction data[34] and integrating these findings with measured implanted hydrogen concentrations (SIMS). First, we provide a detailed description of the studied samples. Next, we examine the depth distributions of hydrogen, damage, and strain as a function of implanted fluences. Finally, we analyze their correlations and investigate the origin of strain in H^+ ion-implanted LTO.

II. SAMPLES AND METHODS

We investigated Y42-cut oriented LTO single crystals, widely employed as substrates for SAW filters (Fig. 1). Commercial wafers, grown by the Czochralski method and provided by Sumitomo Metal Mining, were used. They have a congruent composition of 48.5 mol. % Li_2O and 51.5 mol. % Ta_2O_5. In the particular Y42-cut orientation, the normal to the wafer surface (labeled $\boldsymbol{z'}$ in Fig. 1) makes an angle of 42° with the $[1\bar{1}00]$ axis (labeled $\boldsymbol{y}$) and 90° with the $[\bar{1}\bar{1}20]$ axis (labeled $\boldsymbol{x}$) of the crystal. The piezoelectric axis is inclined at 48° from the surface normal, which deviates from any low-index crystallographic plane [Fig. S1(b)]. Wafers were implanted with H^+ ions at an energy of 110 keV, in a NISSIN iG4HY ion implanter with an incidence angle of 7° from the normal to the surface. During implantation, the temperature was monitored using the electrostatic chuck cooling system and fixed at T = 20 °C. In order to avoid dynamical annealing of the damage, implantation was realized at a low current density of 15 μA cm^{-2}.

The samples were implanted under the same conditions with three different hydrogen fluences, 1.4 × 10^{16} H^+ cm^{-2} (sample

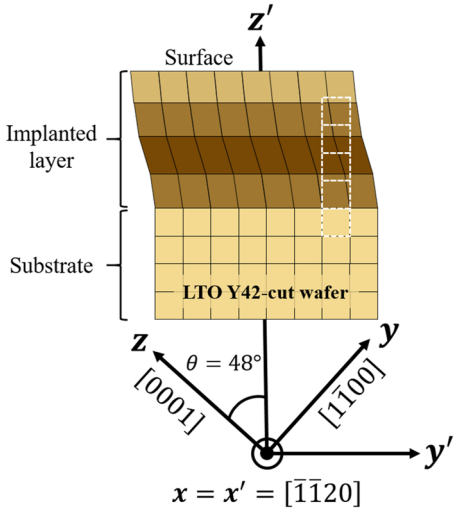

FIG. 1. Continuum body of the implanted LTO Y42-cut wafer viewed along the $[\bar{1}\bar{1}20]$ direction with the *xyz* system of the coordinates related to the LTO crystallographic directions and the user defined $x'y'z'$ right-handed coordinates system associated with the wafer geometry. The dotted white squares represent unstrained continuum body cells corresponding to the pristine LTO bulk structure.

1.4 × 10^{16}), 4 × 10^{16} H$^+$ cm^{-2} (sample **4 × 10^{16}**), and 1 × 10^{17} H$^+$ cm^{-2} (sample **1 × 10^{17}**), later on measured by secondary ion mass spectroscopy (SIMS). The desired fluence was reached through multiple passes of the ion beam over the sample.

Hydrogen concentration depth profiles were extracted by SIMS measurements performed by EAG Laboratories materials characterization service in New Jersey. Cs ions were used as the primary beam, and a quadrupole mass analyzer was used for the detection. Calibrations were carried out using EAG's own reference samples.

Hydrogen and damage profiles were simulated by the SRIM package,[33] using the monolayer collision steps calculation mode. Displacement energies for each chemical element were set to 19.3 eV for Li, 24.4 eV for Ta, and 36.79 eV for O, as calculated in Ref. 35. The total number of simulated ions was limited to 2 × 10^5. These simulations allow the calculation of the H concentration (c_H) profiles normalized by the fluence (f), i.e., $C_H = \frac{c_H}{f}$, and enable to assess the distribution of damage within the implanted layers, represented by a fluence normalized vacancy concentration $\left(C_V^{SRIM} = \frac{c_V}{f}\right)$ profile.

Strain tensor depth profiles in the implanted layers were extracted from high resolution XRD measurements combined with diffractogram simulations by the Radiation Damage in Materials Analyzed with x-ray diffraction (RaDMaX) program.[34] Here, we reconstruct extrinsic strain, i.e., strain defined with reference to the Bravais lattice of LTO crystal following the detailed method already presented in our previous work.[36] Experimental and simulated diffractograms, as well as the deduced corresponding deformation profiles of the $(2\bar{2}04)$ plane (the nearest crystallographic plane aligned with the wafer surface) and the (00012) plane (the plane perpendicular to the c-axis direction) and for the three fluences, are available in the supplementary material [Figs. S2, S3(a), S3(b) and S4(a)–S4(d)].

RaDMaX simulations yield static Debye–Waller (sDW) factor profiles in addition to plane deformation profiles. With appropriate adjustment, these profiles provide a good fit of simulated diffractogram intensities to the experimental ones. The sDW is unit-less and characterizes the damage inside the implanted layers.[34,37] It ranges from 0 to 1, where 1 corresponds to the ideal perfect crystal and 0 corresponds to the amorphous crystal.[34,38,39]

Lamellas for transmission electron microscopy (TEM) were extracted from the implanted wafers and thinned with focused ion beam (FIB) in a FEI Helios Nanolab 600i microscope. We followed the same sample preparation protocol as in Ref. 40, which was specifically adapted to LTO crystals. Lamellas were oriented perpendicular to the $[11\bar{2}0]$ direction.

Atomic resolution scanning transmission electron microscopy (STEM) images were used to measure strain at the local scale. Images were acquired in an FEI Titan 60–300 microscope operated at 300 kV and equipped with a high-brightness Schottky field emission gun (X-FEG) and a CEOS probe aberration corrector. Cross-sectional $(11\bar{2}0)$ images were recorded using a high angle annular dark-field (HAADF) detector, which provides imaging of Ta atomic columns only. The collected HAADF STEM image dataset was processed using the AbStrain method presented in Ref. 41, allowing the measurement of strain tensor components with reference to the Bravais lattice of LTO at different depths of the implanted layer. The detailed protocol and results are presented in the supplementary material (Sec. S2).

Conventional bright-field (BF) TEM images were acquired in a JEOL 2010 microscope equipped with a LaB_6 thermo-ionic electron gun and high contrast objective lens. It was operated at 120 kV to reduce sample damage during observation. BF imaging was performed in two-beam conditions using $g_{1\bar{1}02}$ and slightly out of focus to enhance defects contrast.

III. RESULTS

A. Strain as functions of H concentration and fluence

The additional hydrogen introduced into the crystal is the most evident source of strain in ion-implanted LTO. Consequently, as a first step, we determined the strain tensor component ($\varepsilon_{z'z'}$ and $\varepsilon_{y'z'}$) profiles for the three hydrogen fluences (1.4, 4, and 10 ×10^{16} H$^+$ cm^{-2}) as a function of depth (supplementary material, Fig. S7). Figure 1 illustrates the resulting depth evolution of the shape of the strained implanted LTO, where zero in-plane strain (the implanted region remains pseudomorph to the pristine bulk substrate[36]), gradual tensile out-of-plane strain $\varepsilon_{z'z'}$, and negative shear strain $\varepsilon_{y'z'}$ are schematically represented. In a second step, hydrogen concentration (c_H) profiles as a function of depth were independently measured (Fig. S8). Then, by cross-referencing these two results, we were able to associate the strain values $\varepsilon_{z'z'}$ (solid lines) and $\varepsilon_{y'z'}$ (dashed lines) generated at different depths to the corresponding c_H values for the three samples **1.4 × 10^{16}** (red lines), **4 × 10^{16}** (blue lines), and **1 × 10^{17}** (black lines) [Fig. 2(a)].

All $\varepsilon_{z'z'}$ curves share several common features. To illustrate, we focus on the case of the **1 × 10^{17}** sample (solid black curve). A non-zero value appears just below the surface of the implanted LTO layers at very low H concentration [Fig. 2(a), see insert]. From here, strain amplitude (upper segment of the curve where arrow is pointing to the right) increases with c_H following two quasi-linear regimes until reaching a maximum value at the maximum concentration of H, c_H^{max}. This curve segment reflects the ascending part of the strain and c_H depth profiles (Figs. S7 and S8, respectively). Further into the depth, which corresponds to the descending part of the strain and c_H depth profiles, the curve goes back from c_H^{max} to zero H concentration following the lower segment of the curve [the arrow pointing to the left in Fig. 2(a)]. At the tail of hydrogen depth profile, where $c_H \ll 1$, strain rapidly drops to zero. The negative components $\varepsilon_{y'z'}$ follow similar trends as $\varepsilon_{z'z'}$ components.

Remarkably, for a given fluence, the strain does not have the same value for the same H content corresponding to two depths on either side of a c_H peak. Furthermore, for the different fluences, the strain is not the same for the same H content, increasing as fluence increases. Such a strain-to-H concentration relationship differs a lot from that found in H$^+$ ions implanted Si (001) with fluences ranging from 1 × 10^{16} to 3 × 10^{16} cm^{-2}[14] [Fig. 2(b)]. In Si, strain increases linearly with c_H from zero at low c_H and remains fluence independent. In LTO, a fluence dependent non-zero strain exists already at very low H concentration (at the surface of the wafer). Second, the slopes of the two linear regimes detected for both LTO and Si are different. In LTO, strain increases more rapidly when the H concentration is low, and above a certain c_H threshold value, the rate of strain evolution becomes slower. In Si, the trend is the opposite, with the rate of strain evolution becoming larger for the range of higher H concentration values [see green and red dashed

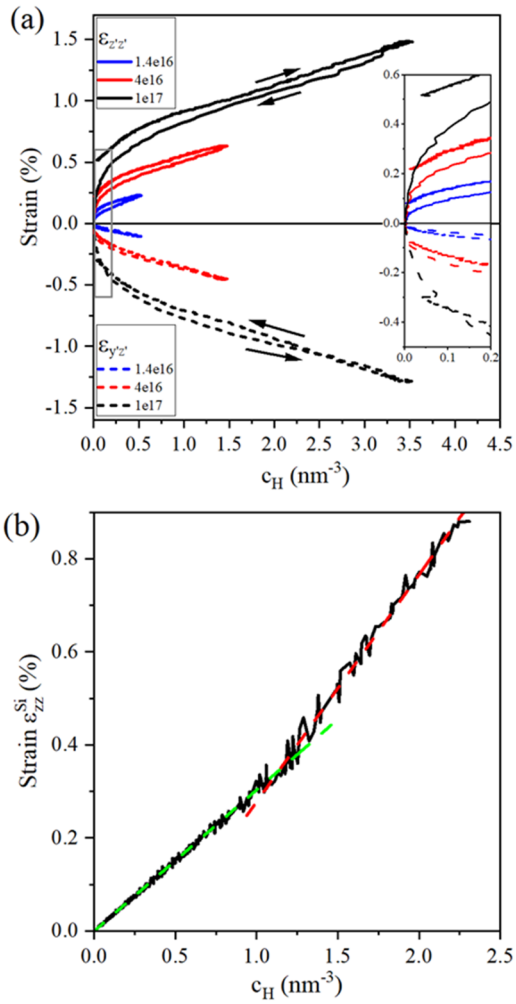

FIG. 2. (a) Strain as a function of hydrogen concentration c_H obtained for the samples **1.4** × **10^{16}** (red lines), **4** × **10^{16}** (blue lines), and **1** × **10^{17}** (black lines). The solid and dashed lines correspond to the out-of-plane and shear strain components, respectively. The arrows represent the direction of increasing depth (only showed for sample **1** × **10^{17}**). The insert shows the zoomed part of (a) for low c_H and (b) out-of-plane strain as a function of c_H obtained in H^+ ions implanted Si (001) with fluences ranging from 1 × 10^{16} to 3 × 10^{16} cm^{-2} (adapted from Ref. 14).

lines in Fig. 2(b), representing the average slopes of the two linear regimes].

Such behaviors of strain evolution with c_H in LTO suggest that H concentration is not the sole contributor to strain. One or more further sources of strain should be taken into account. Damage associated with fluence is likely a significant factor contributing to the overall strain in H^+-implanted LTO. Consequently, we analyzed the evolution of strain with fluence in relation to the amount of generated damage.

B. Strain as a function of damage

Damage profile is typically assumed to be mirrored by the distribution of Li, Ta, and O vacancies, as extracted from the SRIM simulation (noted c_V^{SRIM}). The area under this fluence normalized vacancy profile, A_V^{SRIM}, corresponds to the upper limit for the available number of vacancies since the SRIM does not consider dynamical recombination between vacancies and interstitial atoms. On the another side, the actual shape of the damage profile can be represented by $D(z') = \frac{1-sDW(z')}{f}$ function, where $sDW(z')$ is the Debye–Waller factor profile extracted from the experiment (sDW = 1 corresponds to the perfect crystal). The $D(z')$ function reaches its maximum at maximum damage and is found to be proportional to the fluence (Fig. S10). As it is a unit-less function, we averaged its shape for the different fluences and normalized it by its area A_D and weighted by the area A_V^{SRIM} [Fig. 3(a), green curve]. The resulting fluence normalized damage depth distribution is shown in Fig. 3(a) (black line) and given by

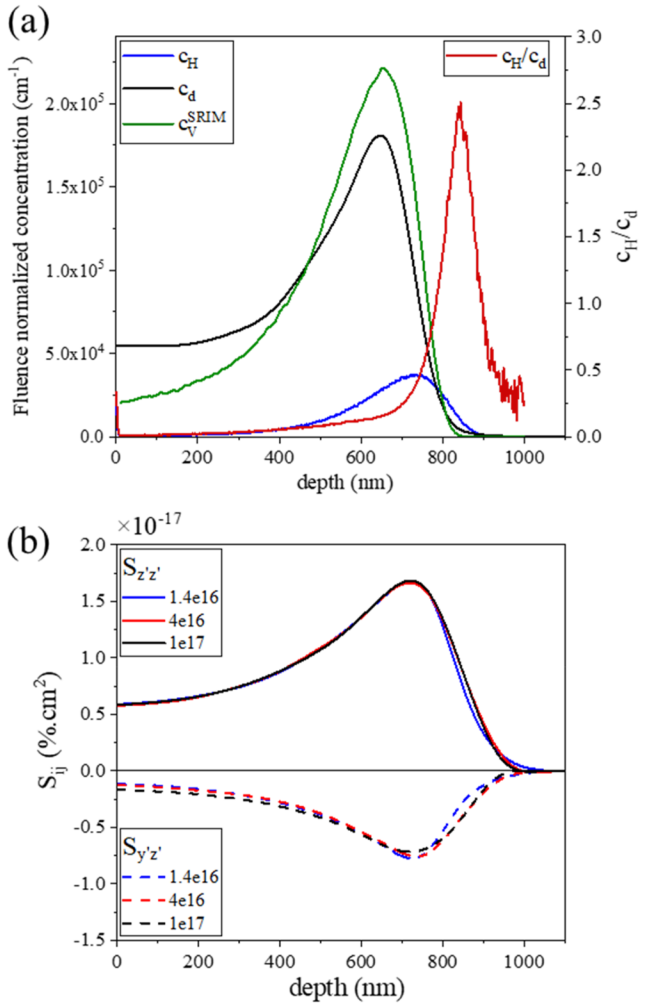

FIG. 3. (a) Fluence normalized profiles of vacancies obtained by SRIM (green line), of damage derived experimentally using Eq. (1) (black line), of hydrogen measured by SIMS, and of ratio $\frac{c_H}{c_d}$ (red line) and (b) shape function of the out-of-plane strain (solid lines) and shear strain (dashed lines) depth profiles, for samples **1.4** × **10^{16}** (blue lines), **4** × **10^{16}** (red lines), and **1** × **10^{17}** (black lines).

$$c_d(z') = D(z')\frac{A_V^{SRIM}}{A_D}. \quad (1)$$

It is worth noting that, contrary to the fluence-normalized hydrogen concentration depth profile c_H [Fig. 3(a), blue line], the damage curves start with non-zero values at the surface and reach a maximum value at a shallower depth of 650 nm than that of the hydrogen peak concentration. Compared with the simulated curve c_V^{SRIM}, the experimentally obtained profile represents more damage in the 400 nm-thick superficial layer and less damage deeper in the substrate. Such a finding is likely to indicate some chemical redistribution of elements after or during ions implantation in LTO, which must be fluence dependent. Up to the damage peak, the damage concentration far outweighs the H concentration. Thus, it is tempting to assume that damage is the main source of strain. Let us verify the proportionality of the strain with the damage.

The damage being normalized by the fluence as SRIM calculated, we need first to normalize the strain by the fluence. When the strain profiles $\varepsilon_{ij}(z', f)$ (Fig. S7) are normalized by their respective fluences f, the resulting curves do not align, indicating a non-linear strain–fluence relationship. However, a strong superposition of the curves is achieved when the strain profiles are normalized by the product $k_{ij}(f)\cdot f$, where $k_{ij}(f)$ is a fluence-dependent, unit-less proportionality factor (unit-less). Figure 3(b) shows the resultant normalized profiles $S_{ij}(z')$ of the out-of-plane and shear strain components given by

$$S_{ij}(z') = \frac{\varepsilon_{ij}(z', f)}{k_{ij}(f).f}, \quad (2)$$

which are plotted for the samples $\mathbf{1.4 \times 10^{16}}$ (blue lines), $\mathbf{4 \times 10^{16}}$ (red lines), and $\mathbf{1 \times 10^{17}}$ (black lines).

The values of the $k_{ij}(f)$ factors are summarized in Table I, where the $k_{ij}(f)$ of the sample $\mathbf{1.4 \times 10^{16}}$ is set to 1. Note that when fluence increases, $k_{z'z'}$ decreases while $k_{y'z'}$ increases.

Such changes in empirical coefficients can plausibly be attributed to variations in the elastic properties of the implanted material, as was found in other H^+ ion implanted materials.[42,43] Those studies showed that different elastic constants change differently when the local hydrogen concentration exceeds a threshold. In particular, the Poisson ratio increases while the shear modulus decreases, meaning the material becomes less compressible. Since the $k_{z'z'}$ decreases and $k_{y'z'}$ increases with fluence in our experiment, we attribute this to similar changes in LTO's elastic constants. In principle, Hooke's law could be used to calculate how the elastic constants change. However, due to the anisotropic structure of LTO and the complexity of the rotated stiffness tensor, there are not enough equations to determine these changes from our data alone. Studying ion implantation in LTO crystals of several orientations, combined with in-plane stress measurements,[43] could help, but this is beyond the scope of the present study.

TABLE I. Strain–fluence proportionality factors.

Sample	$k_{z'z'}(f)$	$k_{y'z'}(f)$
1.4×10^{16}	1	1
4×10^{16}	0.96	1.52
1×10^{17}	0.85	1.73

Because hydrogen is present at a quasi-zero concentration at the surface, $S_{ij}(z')$ can be expressed as a function of damage concentration profile as

$$S_{ij}(z') = \frac{S_{ij}(z'=0)}{c_d(z'=0)}c_d(z'), \quad (3)$$

where $\frac{S_{ij}(z'=0)}{c_d(z'=0)}$ is the rate of normalized strain change with damage concentration, with $S_{z'z'}(z'=0) = 5.8 \times 10^{-18}\%\,\mathrm{cm}^2$ and $c_d(z'=0) = 5.4 \times 10^4\ \mathrm{cm}^{-1}$. However, it is readily apparent that the calculated $S_{ij}(z')$ values significantly surpass the experimental measurements. For example, $S_{z'z'}^{max}$ reaches a value of $1.94 \times 10^{-17}\%\,\mathrm{cm}^2$ at the damage peak of $c_d^{max} = 1.8 \times 10^5\ \mathrm{cm}^{-1}$, which is 30% larger than the value of $1.49 \times 10^{-17}\%\,\mathrm{cm}^2$ found experimentally [Fig. 3(b)]. Moreover, strain continues increasing at the descending part of the damage profile, i.e., maximum damage does not provide the maximum strain. Our findings are corroborated by Ma *et al.*,[32] who showed that, following He^+ ion (heavier than H^+) implantation in LTO, which results in a greater damage and a minuscule content in helium at the wafer surface, strain is not generated. Thus, vacancies or damage alone are unlikely to be the only source of strain in LTO. On the other hand, we note that H cannot be the only source of strain as neither too low H concentration is present at the surface nor strain is fluence dependent. We must conclude that a combination of damage and H atoms is required for strain generation.

C. Strain as a function of hydrogen-to-damage ratio

In order to take into account both species, we divided the H concentration profile by the damage one and obtain the $\frac{c_H}{c_d}$ ratio depth distribution [Fig. 3(a), red line], which is fluence independent. The $\frac{c_H}{c_d}$ begins with a small but non-zero value at the surface, and then quasi-linearly increases until a depth of 640 nm, where damage concentration peaks. Furthermore, the ratio starts to increase more rapidly until reaching the depth of H maximum concentration at 735 nm. Afterward, it grows linearly with a much stronger slope than before until a depth of 840 nm. Finally, the ratio rapidly decreases with depth.

The evolution of the two normalized strain components with $\frac{c_H}{c_d}$ is shown in Fig. 4 and follows four different regimes: (i) linear increase (green zone), (ii) transition regime (cyan zone), (iii) linear decrease (pink zone), and (iv) linear decrease (yellow zone).

Let us analyze the different regimes of $S_{z'z'}$ evolution in relation to the depth and $\frac{c_H}{c_d}$ ratio.

(i) Linear increase $\left(0 < \frac{c_H}{c_d} < 0.14\right)$

This regime corresponds to the depth region extending between the surface $\left(\frac{c_H}{c_d} \ll 1\right)$ and the position of the damage peak $\left(\frac{c_H}{c_d} \approx 0.14\right)$ (green area in Fig. 4). Within this depth range, H and damage concentrations increase monotonically, leading to a linear rise in normalized strain with $\frac{c_H}{c_d}$.

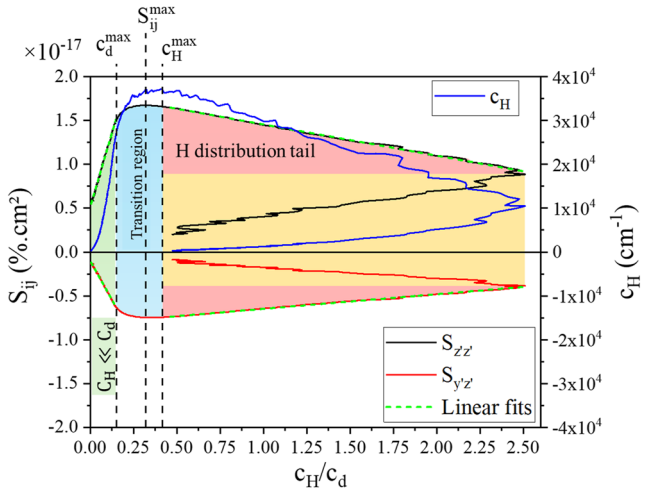

FIG. 4. Out-of-plane (black line) and shear (red line) strain shape functions S_{ij} and the fluence normalized c_H profile (blue line), as a function of the $\frac{c_H}{c_d}$ ratio, for all the samples. The linear fits are indicated by green dashed lines. The damage dominated strain regime is highlighted by the green area, the transition region by the cyan area, and the hydrogen distribution tail by the red and yellow areas.

(ii) Transition region $\left(0.14 < \frac{c_H}{c_d} < 0.41\right)$

This regime corresponds to the depth range between the peak positions of damage and H (cyan area in Fig. 4). There, normalized strain reaches saturation and begins to decline, losing its proportionality to $\frac{c_H}{c_d}$. Up to the H peak depth, strain components rise with H concentration, but their growth rate diminishes as damage concentration decreases. Both $S_{z'z'}(z')$ and $S_{y'z'}(z')$ reach a maximum value of 1.7×10^{-17} and -7.25×10^{-18}% cm^2, respectively, at the H concentration maximum.

(iii) Linear decrease $\left(0.41 < \frac{c_H}{c_d} < 2.5\right)$

This regime corresponds to the descending part of the H depth distribution, i.e., the region deeper than the H peak position (red area in Fig. 4). Strain components decrease linearly with the $\frac{c_H}{c_d}$ ratio. Such a behavior is consistent with a decrease in the concentration of both H and damage. A lower linear slope than that detected in the sub-surface region is related to a slower rate of H concentration decrease with $\frac{c_H}{c_d}$.

(iv) Linear decrease $\left(2.5 > \frac{c_H}{c_d} > 0.41\right)$

This range of $\frac{c_H}{c_d}$ values is inverse to the (iii) regime and corresponds to the H distribution tail at a depth deeper than 840 nm. Here, both H and vacancy concentrations are very small with a range of values similar to that of H in the superficial layer. Strain components decrease linearly with a decrease in $\frac{c_H}{c_d}$ ratio like is found for the (i) regime with a much lower slope. Such a fact is consistent with a small change in H concentration values.

IV. DISCUSSION

The observed evolution of strain components in H^+ ion implanted LTO can be qualitatively interpreted as follows: Strain occurs when H and damage are simultaneously present in the matrix. Hydrogen and point defects incorporation in the LTO unit cell changes its volume and modifies the elastic properties of such a new structure.

The generalized shape function $S_{ij}\left(\frac{c_H}{c_d}\right)$ weighted by both the fluence f and the fluence dependent proportionality coefficient $k_{ij}(f)$ (likely to be related to the modified elastic constants of the material $C_{ijkl}^{LTO^*}$) can be used to calculate the dependence of the absolute strain components as functions of c_H and c_d, which is given by

$$\varepsilon_{ij}(c_H, c_d) = k_{ij}(f) \cdot f \cdot S_{ij}\left(\frac{c_H}{c_d}\right). \quad (4)$$

The strain dependence on fluence is likely to be related to the internal electric fields generated by the as-formed H/damage distribution. The lattice enrichment in interstitial hydrogen and interstitial lattice defects is the first source of the lattice expansion. LTO is a piezoelectric material. When implanted, damaged, and expanded, it is subjected to in-plane compressive stress, which induces tensile out-of-plane and shear strain (through the Poisson effect). This strain induces polarization, creating local electric fields in the implanted regions. These fields follow the strain depth profile. It is expected to generate (increase) the internal electric fields of ~40 kV/cm already existing in the congruent LTO crystals.[44,45] Any increase in the off-stoichiometry would further increase the internal electric fields,[21,44–46] which are expected to act on a part of the damage sensitive to it. To preserve charge neutrality, and because LTO contains charged defects, such as O vacancies and metallic Li atoms, these species redistribute to produce compensating fields. This redistribution explains the observed spatial shift of damage after H^+ implantation in LTO. Hydrogen has a high solubility and bonds with oxygen to form OH^- dipoles. Although they can move under an applied electric field, significant redistribution requires elevated temperatures.[47,48] Comparison between SRIM simulations and SIMS measurements shows no noticeable hydrogen redistribution after implantation, unlike for damage. Therefore, further damage redistribution might be the origin of the strain profile modification. For a given fluence, $\varepsilon_{ij}(c_H, c_d)$ can be different for the same c_H or the same for different c_H as H atoms can be surrounded by a larger or smaller concentration of damage. This explains the asymmetry of the strain profiles with respect to the H peak position.

We can question about the chemical nature of defects encountered in virgin CLT and after implantation. Some information can be found in recent published works. The most stable defect structure in as-grown CLT is a Ta interstitial cluster, which consists of one Ta^{5+} ion on an empty octahedral site surrounded by five Li vacancies V_{Li}^-.[23,49] Hydrogen is also already present in virgin CLT, having been incorporated during the crystal growth process. It tends to preferentially decorate oxygen atoms, forming a configuration, where hydrogen surrounds lithium vacancies V_{Li}^-.[50] Intrinsic H content is determined at 12×10^{17}/cm^3.[25] Extrinsic hydrogen introduced through ion implantation (180 keV, Z-cut, 6, 8, and 10×10^{16} ions/cm^2) has been shown to primarily generate oxygen vacancies and H-ion interstitials in CLT. This leads to lattice distortion, manifesting as an increase in strain within the lattice.[31]

V. CONCLUSION

In this work, we examined the effects of H^+ ion implantation at different fluences and the same energy on the modification of the structural characteristics of LTO, with a focus on identifying the sources of strain generated in the implanted matrix.

By using SIMS, we measured the implanted fluences and extracted fluence normalized H concentration profile. By using XRD measurements and RaDMaX simulations, we measured the strain and damage profiles. We found implanted layers to be pseudomorph to their substrates, gradually tensile strained in the out-of-plane direction and gradually sheared along the piezoelectric axis. We evidenced a clear discrepancy between the SRIM simulated and experimental damage profiles, which indicates damage redistribution following ions implantation in LTO.

By combining damage, H, and strain profiles, we elucidated that strain appears when both H and damage are present in the structure. The strain profiles were found to depend non-linearly on the fluence with the proportionality coefficients dependent on the modified elastic constants. We provided a formula for calculating the out-of-plane and shear strain components in the H^+ ion implanted LTO as functions of hydrogen and damage concentrations by using generalized shape function $S_{ij}\left(\frac{c_H}{c_d}\right)$, which is fluence independent.

The recent studies on the nature of defects in implanted CLT warrant further investigation. Experimental methods previously explored, such as Fourier transform infrared spectroscopy (FTIR) and Raman spectroscopy for hydrogen configuration and concentration, inelastic neutron scattering, nuclear magnetic resonance (NMR) for defect identification, and glow-discharge optical emission spectroscopy (GDOES) for elemental analysis, should be complemented by theoretical calculations, such as density functional theory (DFT). Some theoretical and experimental studies of the elastic constants of H^+ ion implanted LTO can be of interest as well, as their modification could be detrimental for SAW filter applications.

SUPPLEMENTARY MATERIAL

The first section of this supplementary material presents the experimental XRD patterns and the corresponding RaDMaX simulation results for LTO samples implanted with H^+ ions at 110 keV with fluences of 1.4×10^{16} H^+ cm^{-2} ($\mathbf{1.4 \times 10^{16}}$), 4×10^{16} H^+ cm^{-2} ($\mathbf{4 \times 10^{16}}$), and 1×10^{17} H^+ cm^{-2} ($\mathbf{1 \times 10^{17}}$). The second section details the methodology used to quantify the strain components via AbStrain analysis of HAADF HR-STEM images obtained from H^+-implanted LTO samples. The third section compares the depth profiles of the strain tensor components reconstructed from XRD measurements and AbStrain analysis for the different implantation conditions. Subsequent sections present hydrogen depth profiles measured by SIMS and discuss observed artifacts associated with extended defects, as revealed by BF-TEM micrographs. Damage-related (1–*sDW*) curves extracted from the XRD experiments are also shown, confirming the presence and depth distribution of implantation-induced damage within the modified layer, as evidenced by atomic-resolution STEM-HAADF imaging.

ACKNOWLEDGMENTS

The authors acknowledge useful discussions with Didier Landru from Soitec and Alain Claverie and Gérard BenAssayag from CEMES. We also would like to thank the Laboratoire de Physique et Chimie des Nano-objects and the Laboratoire d'analyze et d'architecture des systèmes in Toulouse, France, for providing access to XRD facilities. The part of the work concerning STEM experiments was funded by the Spanish Ministry of Science, Innovation and Universities (Grant No. MCIN/AEI/10.13039/501100011033), through the Severo Ochoa program (Grant No. CEX2023-001286-S), and from Gobierno de Aragon project E13_23R, including FEDER funding. The authors acknowledge the use of instrumentation and the technical advice provided by the National Facility ELECMI ICTS, node "Laboratorio de Microscopías Avanzadas (LMA)" at "Universidad de Zaragoza."

AUTHOR DECLARATIONS

Conflict of Interest

The authors have no conflicts to disclose.

Author Contributions

A. Louiset: Conceptualization (equal); Formal analysis (equal); Investigation (lead); Methodology (equal); Visualization (lead); Writing – original draft (lead); Writing – review & editing (equal). **S. Schamm-Chardon**: Formal analysis (supporting); Funding acquisition (equal); Project administration (equal); Supervision (lead); Writing – review & editing (equal). **O. Kononchuk**: Funding acquisition (equal); Project administration (supporting); Resources (lead); Supervision (supporting); Writing – review & editing (supporting). **C. Magén**: Investigation (supporting); Resources (supporting); Writing – review & editing (supporting). **N. Cherkashin**: Conceptualization (lead); Formal analysis (equal); Funding acquisition (equal); Methodology (equal); Project administration (lead); Resources (lead); Supervision (lead); Visualization (supporting); Writing – original draft (equal); Writing – review & editing (lead).

DATA AVAILABILITY

The data that support the findings of this study are available from the corresponding author upon reasonable request.

REFERENCES

[1] C. C. W. Ruppel, "Acoustic wave filter technology—A review," IEEE Trans. Ultrason. Ferroelectr. Freq. Control **64**(9), 1390–1400 (2017).

[2] K. Y. Hashimoto, M. Kadota, T. Nakao, M. Ueda, M. Miura, H. Nakamura, H. Nakanishi, and K. Suzuki, "Recent development of temperature compensated SAW devices," in *IEEE International Ultrasonics Symposium* (IEEE, 2011), pp. 79–86.

[3] A. Bartasyte, S. Margueron, T. Baron, S. Oliveri, and P. Boulet, "Toward high-quality epitaxial $LiNbO_3$ and $LiTaO_3$ thin films for acoustic and optical applications," Adv. Mater. Interfaces **4**(8), 1600998 (2017).

[4] M. Bruel, B. Aspar, and A.-J. Auberton-Hervé, "Smart-cut: A new silicon on insulator material technology based on hydrogen implantation and wafer bonding," Jpn. J. Appl. Phys. **36**(3S), 1636 (1997).

[5]Y. Yan, K. Huang, H. Zhou, X. Zhao, W. Li, Z. Li, A. Yi *et al.*, "Wafer-scale fabrication of 42° rotated Y-cut $LiTaO_3$-on-insulator (LTOI) substrate for a SAW resonator," ACS Appl. Electron. Mater. **1**(8), 1660–1666 (2019).
[6]E. Butaud, S. Ballandras, M. Bousquet, A. Drouin, B. Tavel, I. Huyet, and A. Reinhardt, "Innovative smart cut^{TM} piezo on insulator (POI) substrates for 5G acoustic filters," in *IEEE International Electron Devices Meeting (IEDM)* (IEEE, 2020), pp. 34–36.
[7]M. Li, M. Qi, Y. Chen, Y. Cheng, L. Cao, and X. Mu, "Suppression of transverse modes in 50°YX-$LiTaO_3$/SiO_2/Si POI SAW resonator with groove configuration," ACS Appl. Mater. Interfaces **16**(35), 46872–46878 (2024).
[8]N. Daghbouj, N. Cherkashin, F. X. Darras, V. Paillard, M. Fnaiech, and A. Claverie, "Effect of the order of He^+ and H^+ ion co-implantation on damage generation and thermal evolution of complexes, platelets, and blisters in silicon," J. Appl. Phys. **119**(13), 135308 (2016).
[9]S. Personnic, K. K. Bourdelle, F. Letertre, A. Tauzin, N. Cherkashin, A. Claverie, R. Fortunier, and H. Klocker, "Impact of the transient formation of molecular hydrogen on the microcrack nucleation and evolution in H-implanted Si (001)," J. Appl. Phys. **103**(2), 023508 (2008).
[10]D. Landru, D. Massy, N. Ben Mohamed, O. Kononchuk, F. Mazen, S. Tardif, and F. Rieutord, "Fracture wake patterns in brittle solids," Phys. Rev. Appl. **15**(2), 024068 (2021).
[11]J. D. Penot, D. Massy, F. Rieutord, F. Mazen, S. Reboh, F. Madeira, L. Capello *et al.*, "Development of microcracks in hydrogen-implanted silicon substrates," J. Appl. Phys. **114**(12), 123513 (2013).
[12]C. Braley, F. Mazen, A. Tauzin, F. Rieutord, C. Deguet, and E. Ntsoenzok, "Si exfoliation by MeV proton implantation," Nucl. Instrum. Methods Phys. Res., Sect. B **277**, 93–97 (2012).
[13]D. S. Chao, Y. C. Hsiao, J. H. Liang, and C. M. Lin, "Effects of crystal plane orientation on blistering kinetics and defect evolution in silicon implanted by hydrogen molecular ions," Surf. Coat. Technol. **394**, 125872 (2020).
[14]N. Cherkashin, F. X. Darras, P. Pochet, S. Reboh, N. Ratel-Ramond, and A. Claverie, "Modelling of point defect complex formation and its application to H^+ ion implanted silicon," Acta Mater. **99**, 187–195 (2015).
[15]N. Sousbie, L. Capello, J. Eymery, F. Rieutord, and C. Lagahe, "X-ray scattering study of hydrogen implantation in silicon," J. Appl. Phys. **99**(10), 103509 (2006).
[16]M. Nastasi, T. Höchbauer, J. K. Lee, A. Misra, J. P. Hirth, M. Ridgway, and T. Lafford, "Nucleation and growth of platelets in hydrogen-ion-implanted silicon," Appl. Phys. Lett. **86**(15), 154102 (2005).
[17]J. K. Lee, Y. Lin, Q. X. Jia, T. Höchbauer, H. S. Jung, L. Shao, A. Misra, and M. Nastasi, "Role of strain in the blistering of hydrogen-implanted silicon," Appl. Phys. Lett. **89**(10), 101901 (2006).
[18]A. Tauzin, J. Dechamp, F. Madeira, F. Mazen, M. Zussy, C. Deguet, L. Clavelier, J. S. Moulet, C. Richtarch, T. Akatsu, M. Yoshimi, and A. Rigny, "3-inch single-crystal $LiTaO_3$ films onto metallic electrode using smart cut^{TM} technology," Electron. Lett. **44**(13), 822–824 (2008).
[19]W. Liu, D. Zhan, X. Ma, Z. Song, and S. Feng, "Fabrication of single-crystalline $LiTaO_3$ film on silicon substrate using thin film transfer technology," J. Vac. Sci. Technol. B **26**(1), 206–208 (2008).
[20]R. Hsu, E. N. Maslen, D. Du Boulay, and N. Ishizawa, "Synchrotron X-ray studies of $LiNbO_3$ and $LiTaO_3$," Acta Crystallogr., Sect. B **53**(3), 420–428 (1997).
[21]S. Aoyagi, H. Osawa, K. Sugimoto, M. Iwata, S. Takeda, C. Moriyoshi, and Y. Kuroiwa, "Crystal structure analysis of $LiTaO_3$ under electric field," Jpn. J. Appl. Phys. **54**(10S), 10NB03 (2015).
[22]S. Kim, V. Gopalan, K. Kitamura, and Y. Furukawa, "Domain reversal and nonstoichiometry in lithium tantalate," J. Appl. Phys. **90**(6), 2949–2963 (2001).
[23]A. Vyalikh, M. Zschornak, T. Köhler, M. Nentwich, T. Weigel, J. Hanzig, R. Zaripov *et al.*, "Analysis of the defect clusters in congruent lithium tantalate," Phys. Rev. Mater. **2**(1), 013804 (2018).
[24]A. V. Yatsenko, M. N. Palatnikov, and N. V. Sidorov, "Investigation of the intrinsic defects of $LiTaO_3$ crystals by NMR spectroscopy," Crystallogr. Rep. **64**, 36–40 (2019).
[25]T. Köhler, P. Reichart, E. Brendler, A. Vyalikh, A. Klostermeier, Z. Siketić, E. Mehner *et al.*, "On the quantification of hydrogen in lithium metal oxides," J. Mater. Chem. A **11**(39), 21183–21202 (2023).
[26]P. J. Matthews, A. R. Mickelson, and S. W. Novak, "Properties of proton exchange waveguides in lithium tantalate," J. Appl. Phys. **72**(7), 2562–2574 (1992).
[27]V. A. Fedorov and Y. Korkishko, "Crystal structure and optical properties of proton-exchanged $LiTaO_3$ waveguides," Ferroelectrics **160**(1), 185–208 (1994).
[28]C. E. Rice and J. L. Jackel, "$HNbO_3$ and $HTaO_3$: New cubic perovskites prepared from $LiNbO_3$ and $LiTaO_3$ via ion exchange," J. Solid State Chem. **41**(3), 308–314 (1982).
[29]N. Cherkashin, S. Reboh, M. J. Hÿtch, and A. Claverie, "Strain in hydrogen-implanted Si investigated using dark-field electron holography," Appl. Phys. Express **6**(9), 091301 (2013).
[30]Z. Li, K. Huang, Y. Ji, Y. Chen, X. Zhao, M. Zhou, T. You *et al.*, "Investigations on ion implantation-induced strain in rotated Y-cut $LiNbO_3$ and $LiTaO_3$," Chin. Phys. B **30**(10), 106103 (2021).
[31]K. Zhang, W. Luo, X. Zeng, S. Huang, L. Wan, Y. Shuai, C. Wu, and W. Zhang, "Ion implantation caused defects and their effects on $LiTaO_3$ crystal exfoliation," Phys. Status Solidi A **219**(8), 2100720 (2022).
[32]C. Ma, F. Lu, B. Xu, and R. Fan, "Visualized strain profile in the process of crystal ion slicing of $LiTaO_3$," J. Phys. D: Appl. Phys. **49**(20), 205301 (2016).
[33]J. F. Ziegler and J. P. Biersack, "The stopping and range of ions in matter," in *Treatise on Heavy-Ion Science* (Springer, Boston, 1985), pp. 93–129.
[34]M. Souilah, A. Boulle, and A. Debelle, "*RaDMaX*: A graphical program for the determination of strain and damage profiles in irradiated crystals," J. Appl. Crystallogr. **49**(1), 311–316 (2016).
[35]B. A. Petersen, *Low Energy Recoil Simulations in MgO, $LiNbO_3$, and $LiTaO_3$ Using Ab Initio Molecular Dynamics* (University of Tennessee, Knoxville, 2017).
[36]A. Louiset, S. Schamm-Chardon, O. Kononchuk, and N. Cherkashin, "Reconstruction of depth resolved strain tensor in off-axis single crystals: Application to H^+ ions implanted $LiTaO_3$," Appl. Phys. Lett. **118**(8), 082903 (2021).
[37]N. Kato, "Statistical dynamical theory of crystal diffraction. I. General formulation," Acta Crystallogr., Sect. A **36**(5), 763–769 (1980).
[38]P. Becker and M. Al Haddad, "Diffraction by a randomly distorted crystal. I. The case of short-range order," Acta Crystallogr., Sect. A **46**(2), 123–129 (1990).
[39]J. P. Guigay and F. N. Chukhovskii, "Reformulation of the statistical theory of dynamical diffraction in the case E = 0," Acta Crystallogr., Sect. A **51**(3), 288–294 (1995).
[40]M. Schaffer, B. Schaffer, and Q. Ramasse, "Sample preparation for atomic-resolution STEM at low voltages by FIB," Ultramicroscopy **114**, 62–71 (2012).
[41]N. Cherkashin, A. Louiset, A. Chmielewski, D. J. Kim, C. Dubourdieu, and S. Schamm-Chardon, "Quantitative mapping of strain and displacement fields over HR-TEM and HR-STEM images of crystals with reference to a virtual lattice," Ultramicroscopy **253**, 113778 (2023).
[42]F. Rieutord, F. Mazen, S. Reboh, J. D. Penot, L. Bilteanu, J. P. Crocombette, V. Vales *et al.*, "Lattice strain of hydrogen-implanted silicon: Correlation between X-ray scattering analysis and *ab-initio* simulations," J. Appl. Phys. **113**(15), 153511 (2013).
[43]S. Reboh, F. Rieutord, L. Vignoud, F. Mazen, N. Cherkashin, M. Zussy, D. Landru, and C. Deguet, "Effect of H-implantation in the local elastic properties of silicon crystals," Appl. Phys. Lett. **103**(18), 181911 (2013).
[44]V. Gopalan and M. C. Gupta, "Origin of internal field and visualization of 180 domains in congruent $LiTaO_3$ crystals," J. Appl. Phys. **80**(11), 6099–6106 (1996).
[45]L. Tian, V. Gopalan, and L. Galambos, "Domain reversal in stoichiometric $LiTaO_3$ prepared by vapor transport equilibration," Appl. Phys. Lett. **85**(19), 4445–4447 (2004).
[46]K. Kitamura, Y. Furukawa, K. Niwa, V. Gopalan, and T. E. Mitchell, "Crystal growth and low coercive field 180 domain switching

characteristics of stoichiometric $LiTaO_3$," Appl. Phys. Lett. **73**(21), 3073–3075 (1998).
[47]R. González and Y. Chen, "Transport of hydrogenic species in crystalline oxides: Radiation and electric-field-enhanced diffusion," J. Phys.: Condens. Matter **14**(45), R1143 (2002).
[48]T. J. Wang, C. F. Huang, W. S. Wang, and P. K. Wei, "A novel wet-etching method using electric-field-assisted proton exchange in $LiNbO_3$," J. Lightwave Technol. **22**(7), 1764 (2004).
[49]T. Köhler, M. Zschornak, M. Zbiri, J. Hanzig, C. Röder, C. Funke, and D. C. Meyer, "Defect formation in chemically reduced congruent $LiTaO_3$: *Ab initio* simulations and inelastic neutron scattering," J. Mater. Chem. C **9**(38), 13484–13499 (2021).
[50]T. Köhler, M. Zschornak, C. Röder, J. Hanzig, G. Gärtner, T. Leisegang, E. Mehner, H. Stöcker, and D. C. Meyer, "Chemical environment and occupation sites of hydrogen in $LiMO_3$," J. Mater. Chem. C **11**(2), 520–538 (2023).